

Heat loss and internal dynamics of Venus from global surface heat flow estimates

Javier Ruiz^{1,*}, Alberto Jiménez-Díaz², Isabel Egea-González³,
Ignacio Romeo¹, Jon F. Kirby⁴, Pascal Audet⁵

¹ Departamento de Geodinámica, Estratigrafía y Paleontología; Facultad de Ciencias Geológicas, Universidad Complutense de Madrid, 28040 Madrid, Spain

² Departamento de Biología y Geología, Física y Química Inorgánica. ESCET, Universidad Rey Juan Carlos, 28933 Móstoles, Madrid, Spain

³ Departamento de Física Aplicada. Escuela Superior de Ingeniería. Universidad de Cádiz, 11519 Puerto Real, Cádiz, Spain

⁴ School of Earth and Planetary Sciences, Curtin University, GPO Box U1987, Perth WA 6845, Australia

⁵ Department of Earth and Environmental Sciences, University of Ottawa, Ottawa, Ontario, Canada

* Corresponding author. E-mail: jaruiz@ucm.es

ABSTRACT

The absence of plate tectonics and the young surface age (0.3-1 billion years) of Venus have led to diverse geodynamic models for Venus. The energetics of the Venusian interior drive these models; however, the lack of direct constraints on surface heat flow hampers their quantitative assessment. Here we present the first global heat flow map for Venus, obtained from an inversion of geophysical data, including crustal thickness, effective elastic thickness, and radioactive heat production. Heat flow on Venus is lower and less geographically structured than on Earth but with highs reaching values typical of magmatically active terrestrial areas. The obtained total heat loss is 11-14.5 TW, similar to estimates of the total radioactive heat production. Therefore, at present, Venus proportionally dissipates much less heat than Earth. Furthermore, the calculated crustal temperatures imply that crustal melting or eclogitization are not dominant in the Venusian crust.

INTRODUCTION

Despite their similar size and mass, Earth and Venus have very different internal dynamics that reflect contrasting modes of heat loss. On Earth, plate tectonics drives heat loss through rigid plate recycling^{1,2}, with a minor contribution from mantle plume (i.e. hot spot) activity. This creates significant topography and a structured surface heat flow distribution, with high and low heat flow corresponding to mid-ocean ridges and old continental cores, respectively. In comparison, the surface of Venus is more homogeneous, has lower relief, and shows evidence of effusive volcanism. Models of the internal dynamics sought to explain these observations invoke a variety of processes³: The surface lid could be mostly sluggish with limited lithosphere movement⁴. Heat loss could be dominated by plume and rifting activity, raising significant amounts of volcanism or plutonism⁵, which could even make the lithosphere squishy and fragmented⁶. Venus could be operating in an “episodic mode” alternating stagnant lid and lithosphere wholesale recycling (including outbursts of subduction and/or magmatism)^{7,8}, or even as a mix of processes in space and/or time⁹⁻¹². Furthermore, early giant collisions might have had a significant role in the duration of volcanism and resurfacing¹³. However, the lack of constraints on heat loss from direct surface heat flow measurements for Venus hampers a quantitative appraisal of these models.

Surface heat flow can be estimated using proxies for the thermal structure of the lithosphere derived from satellite data. On Venus, local and regional estimates are obtained from modeling lithospheric flexure¹⁴⁻¹⁸, the depth to the brittle-ductile transition¹⁹⁻²¹, and topographic and crustal relaxation^{22,23}. Average surface heat flow values are calculated using mass/radius scaling based on terrestrial heat flow or radioactive heat production²⁴⁻²⁶, which requires assuming (explicitly or implicitly) similar dynamics for both planets. These estimates provide local and regional constraints on heat flow but cumulatively cover only a small surface area.

In this study, we use a model describing the spatial variations of the effective elastic thickness of the lithosphere (T_e) to generate the first global, $2^\circ \times 2^\circ$ surface heat flow map for Venus. Calculated heat flow values must be considered upper limits and represent the thermal state when the long-wavelength relation between topography and gravity was established. Because the Venusian surface is young²⁷, our map is representative of the thermal state of Venus in recent times (see Discussion). Using these data, we calculate upper limits for the total heat loss for Venus, which can be compared with geochemical information and Earth-based scaling. These estimates provide quantitative constraints for the appraisal of geodynamic models of Venus.

RESULTS

Heat flow map

To derive our heat flow map, we use an updated version of the global map of the effective elastic thickness of the lithosphere by Jiménez-Díaz et al.²⁸ (Fig. 1). This model is constructed by inverting the spectral relations between gravity and topography data calculated with the wavelet method (see Methods). Surface heat flow values were derived from a model relating T_e and the temperature-dependent lithospheric strength envelope^{29,30} and constraints from a global crustal model (Fig. S1). We assume zero bending moment for the lithosphere, which implies that the calculated heat flow values are upper bounds (see Methods), useful for constraining planetary thermal evolution³⁰.

Our model considers a basaltic crust for Venus^{31,32}, with an appropriate nominal density of 2900 kg m^{-3} , and thermal conductivity of $2 \text{ W m}^{-1} \text{ K}^{-1}$. The possibility of a more felsic composition for crustal plateaus has been suggested³³⁻³⁵ but its effect on total heat loss calculations would be minimal (see Discussion). Our model also considers crustal heat sources, which increases the calculated heat flow for a given T_e (ref. 30), consistent with upper limit calculations. We use $0.4 \mu\text{W m}^{-3}$ for the average radioactive heat production based on measurements from Venera and Vega landers³⁶ (see Methods).

The recovered heat flow data (Fig. 2a) have minimum and maximum values of 18 and 148 mW m^{-2} respectively, and an average value of 30.3 mW m^{-2} . The $2^\circ \times 2^\circ$ map shows large-scale areas with either high or low heat flow values: high values ($>35 \text{ mW m}^{-2}$) are mainly found on the regional volcanic plains, including Guinevere, Atlanta, Akhtamar, Tahmina, Sedna and Lavinia Planitiae; low values ($<26 \text{ mW m}^{-2}$) are found on Himenoa Planitia and Themis Regio in the region known as the BAT anomaly area³⁷, and on the regional plains of Northern Nsomeka and Aino Planitiae; intermediate values ($26\text{-}35 \text{ mW m}^{-2}$) characterize Niobe planitia and the highlands of Aphrodite and Ishtar Terrae. The map shows smooth large-scale variations compared to those observed in a global map of the terrestrial heat flow at the same resolution (Fig. 2b). The uncertainties in heat flow estimates derived from the uncertainty in T_e determination are small (Fig. S2), with an average of 0.8 mW m^{-2} , and reaching 9 mW m^{-2} for the highest heat flow values but never

exceeding 6%.

The ratio between maximum and minimum values obtained for Venus is lower than ten, whereas the same ratio for the Earth is much higher (see Methods). This may partly result from the smoothing effect of using T_e -derived estimates of heat flow distribution on Venus, as opposed to direct heat flow measurements on Earth. However, the geographical heat flow pattern of Earth is consistent with the predictions from several geophysical proxies², whereas the geographical pattern of Venusian is very different and less structured. Thus, Venus lost heat more homogeneously than Earth, whose interior cooling pattern is a direct consequence of plate tectonics.

Total heat loss

We use our heat flow map to calculate a total heat loss of 13.9 TW for Venus. Considering the uncertainty in T_e determination, the total heat loss could be between 13.6 and 14.3 TW. Otherwise, if crustal heat sources are not considered (i.e., using linear thermal gradients), the total heat loss fall to 11.0 TW (and the average heat flow to 24 mW m⁻²).

The total heat loss obtained here is much lower than the terrestrial values scaled to Venus. Scaling the updated estimate for Earth of 40-42 TW (ref. 2) to Venus would give 33-34 TW. The terrestrial total heat loss is much higher than the radioactive heat production, which lies between 14 and 20 TW, depending on the geochemical model considered³⁸⁻⁴¹ (see Methods). Thus, Earth is losing two or three times more heat than radioactively produced, which implies vigorous interior cooling. If we scale the terrestrial radioactive heat production to Venus we obtain a range between 11 and 16 TW. Heat loss and radioactive heat production values are therefore comparable for Venus: the heat loss of this planet would be, at most, around 30% higher than its heat production but could be lower. This can be expressed in terms of the bulk Urey ratio, defined for a bulk planet as the ratio between the total radiogenic heat production and the total surface heat loss⁴². Whereas this value for the Earth is 0.3-0.5, we obtain a value higher than 0.7-0.8 for Venus, implying that the bulk interior of this planet is moderately cooling down or even heating up.

Temperature at the base of the crust

Under particular conditions, large-scale basalt melting¹⁷, or eclogitization and associated delamination⁴³, can occur in the lower crust. This might affect the stability of the crustal structure and, therefore, the consistency and validity of our results. We calculate the temperature at the base of the crust from our nominal heat flow results (see Fig. S3) and find temperatures exceeding the basalt solidus or liquidus (see Methods) only in rare cases (see Fig 3, S4a and S4b). Therefore, our analysis does not predict large-scale melting of the crust. Since our heat flow calculations are upper limits, the actual crustal thermal profile may not reach the basalt solidus at these locations. Similarly, eclogitization is not expected

for our temperature profiles (see Fig. 3). The basalt-eclogite transition would occur for crustal thickness greater than about 40 km and temperatures at the base of the crust higher than 673 K. Our crustal model provides some locations with a crustal thickness greater than 40 km, but the temperature at the base of the crust exceeds the temperature at which the eclogite transition takes place. Thus, our regional heat flow estimates (and hence the total heat loss of Venus) are consistent with crustal stability.

DISCUSSION

Our results reveal that the interior dynamics of Venus is very different from that of the Earth based on both global heat budget and heat flow geographical distribution. Indeed, we show that Venus loses proportionally less heat than Earth, with much lower relative variation across its surface. The estimated heat flows span a wide range of values including those obtained by previous works for specific features or terrains on Venus^{14,17,21,22}. Some works^{15,16,18} used high values for the thermal conductivity of the crust or the entire mechanical lithosphere, which proportionally raised their calculated heat flows. Therefore a proper comparison with these works requires considering this. Whereas average values are comparatively low, our higher heat flow estimates can be as high as 150-160 mW m⁻², consistent with results previously obtained for zones characterized by coronae, rift systems or ribbon terrains¹⁸⁻²⁰. These features correspond to (past or present) actively deforming lithosphere with higher-than-average expected heat flow. However, as in the case of Earth (e.g., around hotspots), very localized highs do not significantly contribute to the total heat loss.

Some geographical differences in heat flow may be related to age variations between regions. Because of the relatively young surface of Venus (~300-1000 Ma on average²⁷), these age differences should not be higher than a few hundred Ma. This time is comparable to the thermal time of the mechanical lithosphere, and therefore our map is informative of the last hundreds of millions of years of the planet. The thermal time is a rough estimate of the time for thermal perturbations to be dissipated out through heat diffusion: taking a standard heat diffusivity value for rocks of $\sim 10^{-6} \text{ m}^2 \text{ s}^{-1}$, the thermal time would be $\sim 10^2$ Ma for a lithosphere ~ 50 -100 km thick. The mechanical lithosphere is the real layer supporting geological stresses and is usually thicker than the effective elastic thickness; for a thick and unbent lithosphere, the mechanical and effective elastic thicknesses are similar^{29,44} (see Methods).

The effective elastic thickness is representative of the time when the topography and gravity signals were established⁴⁵. Therefore, there cannot be subsequent lithosphere heating, since it would imply lithosphere thinning and T_e reduction. Later cooling and lithosphere thickening cannot be detected through T_e analysis. Whichever potential process that can lower T_e in a non-thermal way (e.g., stress relaxation) would result in an overestimation of the calculated heat flow. Thus, the implications of our results for the global dynamics of Venus are robust: both the calculated heat flow and their geographical

variations are upper limits. Our model considers a basaltic crust for Venus. A felsic component in crustal plateaus should not significantly affect our conclusions. On one hand, the thermal conductivity of both felsic and basic crustal rocks at several hundreds of Celsius degrees is around $2 \text{ W m}^{-1} \text{ K}^{-1}$ (see Methods), and therefore the effect of a felsic component on the average thermal conductivity of the Venusian crust could be not significant; on the other hand, a felsic component would imply a proportionally weaker crust and a lower heat flow for a given T_e .

Fig. 4a shows the inverse of the bulk Urey ratio as a function of the total radioactive heat production of Venus; the inverse of the Urey ratio offers a more visual perspective of the amount of internal cooling/heating of a planet (for a version shown in terms of the bulk Venus Urey ratio see Fig. S5). The nominal total heat loss of Venus is set to 14.0 TW, but we also show the case for a heat loss of 14.5 TW (which can be taken as a robust upper limit for the total heat loss of Venus considering the uncertainty in T_e determination). The total radioactive heat production is calculated for the range deduced from terrestrial-based compositional scaling. Higher and lower total radioactive heat production values correspond to, respectively, chondritic and subchondritic compositions (see Methods sections). Because our heat flow map gives upper limits, the calculated inverse Urey ratios give an upper limit to the proportion between heat loss and radiogenic heat production and, therefore, to the amount of interior cooling (or conversely, a lower limit to the interior heating). For a total heat production of 14-14.5 TW or higher, the bulk Venusian interior would necessarily be heating up at present. The possibility of a sub-chondritic composition for the terrestrial planets, maybe related to early heavy erasing of their crusts by giant impacts, would be consistent with isotopic and mass balance evidence⁴⁶, and with the secular evolution of the temperature of the terrestrial mantle⁴⁷.

The used crustal radioactive heat production of $0.4 \mu\text{W m}^{-3}$ provides a reasonable upper limit for Venus, but the actual value is not well known. Fig.4a and S5 also show the case without crustal heat sources. In this case, the interior is always heating up. Fig. 4b shows, in terms of the crustal heat production rate, the total heat loss of Venus, the crustal contribution, and the mantle heat loss (given by the difference between both). We observe that the variation of the mantle heat loss is relatively small, between 9.4 and 11.0 TW, for the considered range of heat production. Thus, the nominal value of crustal heat production used here should not substantially influence the implications of our work for the dynamics of the Venusian mantle.

Large-scale geological structures are very different on Earth and Venus despite similar size and bulk properties. Earth shows tectonic structures mostly associated with plate boundaries⁴⁸, while the global tectonic pattern of Venus is characterized by distributed deformation and much more limited lithosphere subduction or spreading^{18,49}. Our results show that from a thermal perspective, Venus is operating in its unique mode, which is globally less efficient in transmitting heat through the lithosphere than present-day terrestrial plate tectonics. Plate tectonics is a self-sustained process that efficiently cools the mantle and reduces the viscosity contrast across the silicate layer, which in turn favors a

coupled lithosphere-convective interior⁴⁶. Without global plate tectonics, interior cooling is less efficient, thus lowering lithosphere-convective coupling. In these conditions, other processes of heat transfer must be important.

Our heat flow model offers two important thermal constraints for understanding the Venusian dynamics, and successful interior evolution models should be consistent with them. Our results show that the geographical pattern of heat flow on Venus is less structured than on Earth and that, during the last hundreds of million years, the heat loss of Venus was roughly comparable to its radioactive heat production and that the interior cooling was, at most, limited.

METHODS

Crustal (T_c) and effective elastic thickness (T_e) maps

We use the crustal thickness (T_c) model from Jiménez-Díaz et al.²⁸ and an updated version of the effective elastic thickness (T_e) model of these authors, derived both from gravity and topography data and averaged onto $2^\circ \times 2^\circ$ grids. The topography and gravity data were obtained from the spherical harmonic models SHTJV360u (ref. 51) and SHGJ180u (ref. 52) respectively. Both spherical harmonic models were truncated to degree and order 180.

The crustal thickness model was obtained following the potential theory procedure^{50,53}. This procedure first calculates the Bouguer gravity anomaly from surface topography and the free air anomaly, and then calculates, by downward continuation, the shape of the crust-mantle interface necessary to minimize the difference between the observed and predicted Bouguer anomalies. The crustal thickness was constrained assuming (1) observed gravitational anomalies arising only from relief along the surface and crust-mantle interface, and (2) constant crustal and mantle densities. The model assumes a mean crustal thickness of 25 km, and crust and mantle densities of, respectively, 2900 and 3300 kg m⁻³. To mitigate errors in the downward continuation of Bouguer anomalies, a minimum amplitude filter at degree $l = 70$ is applied. Finally, the crustal thickness was obtained by subtracting the relief along the crust-mantle interface from the surface topography (see Fig. S1).

The crustal thickness of Venus is not well known. The assumed mean crustal thickness of 25 km is consistent with numerical models of rifting in Venus⁵⁴. Our assumed mean crustal thickness is somewhat higher than the mean value of 22 km favored by Maia and Wiczorek¹⁷ from Airy isostasy of crustal plateaus, although a standard deviation of ± 5 km would be obtained from the mean crustal thickness values deduced by these authors from several crustal plateaus (giving a total range between 17 and 27 km).

The effective elastic thickness model was obtained from the inversion of the

Bouguer coherence function using the fan wavelet transform^{55,56}, modeled with a simple thin elastic plate subject to both surface and subsurface loads, following the load deconvolution procedure of Forsyth⁵⁷. The wavelet method provides a coherence estimate at every point on the data grid. The analysis was performed in the Cartesian domain, dividing the surface of Venus into 36 overlapping areas (or ‘tiles’), and projecting the gravity and topography in each of them to a Cartesian frame using an oblique Mercator map projection. The planar wavelet analysis for coherence and the T_e inversion were then carried out for each tile.

The inversion for T_e by Jiménez-Díaz et al.²⁸ was performed only on observed coherences with wavelengths >211 km. This corresponds to a flexural wavelength such that the minimum resolvable T_e is ~ 14 km (see ref. 28 for details), which, therefore, imposes an upper limit on the calculated heat flow. Therefore, we carry out the inversion for the complete range of available and resolvable wavelet scales (equivalent Fourier wavelengths). The largest scale was chosen such that the longest equivalent Fourier wavelength was 6000 km (the side length of a tile); the smallest chosen scale corresponds approximately to the Nyquist wavelength of the gridded data (40 km; see ref. 28), which, if taken as a flexural wavelength, implies a minimum resolvable T_e of ~ 2 km. After inversion, T_e data at the edges of each tile (ten percent of a side length) were removed to mitigate possible remnant edge effects near the grid boundaries. As a final step, T_e results were back-projected onto a geographic $1^\circ \times 1^\circ$ grid and merged and gridded to produce a global map that combines the information from all tiles. The uncertainty in the determination of T_e , given as 95% confidence limits on the best-fitting value, is shown in Fig. S2a.

Heat flow and temperature profile calculation

We use the effective elastic thickness of the lithosphere (T_e) to constrain a lithospheric temperature profile and thus surface heat flow^{29,30}. In the following derivation, we use an asterisk (*) to describe a modeled (as opposed to observed or estimated) elastic thickness.

Flexural stresses can exceed the strength of rocks at both the top and bottom of the plate^{44,58,59}. At shallow depths, the brittle strength of rocks is determined by Byerlee’s rule, whereas at deeper levels, rheology is described by power-law creep, which is temperature-dependent. The depth at which ductile strength reaches a given small value (and below which strength does not increase again) can be used to define a mechanical thickness, T_m . T_e^* can then be related to T_m by vertically integrating the lesser of yield and bending stresses for a given plate curvature, effectively calculating the bending moment¹⁸. Here we assume that plate curvature is small (zero bending moment), which implies that $T_e^* \approx T_m$ for each layer. This gives an upper limit to the calculated heat flow, which is useful for our purposes³⁰.

The power law describing ductile strength is

$$(\sigma_1 - \sigma_3)_d = \left(\frac{\dot{\epsilon}}{A} \right)^{1/3} \exp\left(\frac{Q}{nRT} \right), \quad (1)$$

where $\dot{\epsilon}$ is the strain rate, A , Q , and n are empirically determined constants, R ($= 8.31446 \text{ J mol}^{-1} \text{ K}^{-1}$) is the gas constant, and T is the absolute temperature. Here, we use a strain rate of 10^{-16} s^{-1} in the calculations: this is a typical strain rate for active terrestrial plate interiors⁶⁰, and it is a reasonable upper limit for the recent tectonic activity of Venus⁶¹. We assume 10 MPa as the strength value defining the base of T_m (refs. 30, 62).

We model the Venusian lithosphere as two homogeneous layers representing the crust and mantle. For creep parameters of the crust, we use constants for a flow law for dry diabase²⁰: $A = 30 \text{ MPa}^{-n} \text{ s}^{-1}$, $n = 4.7$ and $Q = 485 \text{ kJ mol}^{-1}$; these parameter values give the mean strength between those obtained for dry Columbia and Maryland diabases according to experimental flow laws⁶³. The ductile strength of the mantle lithosphere is calculated for dry olivine dislocation creep rheology, using a flow law for dry dunites⁶⁴: $A = 28840 \text{ MPa}^{-n} \text{ s}^{-1}$, $n = 3.6$ and $Q = 535 \text{ kJ mol}^{-1}$.

A weak lower crust may allow a mechanical decoupling between crust and mantle. We define decoupling by deviatoric stresses at the base of the crust lower than 10 MPa. In this case T_e^* is estimated by⁶⁵

$$T_e^* \approx \left[(T_{e,c}^*)^3 + (T_{e,m}^*)^3 \right]^{1/3}, \quad (2)$$

otherwise the crust and mantle behave as a single unit and T_e^* is estimated by⁶⁵

$$T_e^* \approx T_{e,c}^* + T_{e,m}^*. \quad (3)$$

Decoupling will generally occur where the crust is thick and temperatures at lower crustal depths are elevated.

Temperature profiles in the crust are calculated by assuming a homogeneous distribution of radioactive heat sources, and therefore the temperature at a given depth z is given by

$$T_{z,c} = T_s + \frac{F_s z}{k_c} - \frac{H_c z^2}{2k_c}, \quad (4)$$

where T_s is the surface temperature, F_s is the surface heat flow, k_c is the thermal conductivity of the crust, and H_c is the volumetric heating rate of the crust. We use a surface temperature of 740 K, a value of $0.4 \mu\text{W m}^{-3}$ for the heat production of the crust

(see next section), and a thermal conductivity of $2 \text{ W m}^{-1} \text{ K}^{-1}$, a standard value appropriate for basaltic rocks⁶⁶. Furthermore, the thermal conductivity of felsic and basic crustal rocks at several hundreds of Celsius degrees is around $2 \text{ W m}^{-1} \text{ K}^{-1}$ (refs. 67,68). For this reason, this value is useful here, even considering a felsic component for the Venusian crust. We calculate temperature profiles in the mantle lithosphere using

$$T_{z,m} = T_{cb} + \frac{F_m(z - T_c)}{k_m}, \quad (5)$$

where T_{cb} is the temperature at the base of the crust, $F_m = F_s - H_c T_c$ is the mantle heat flow, T_c is the thickness of the crust, and k_m is the thermal conductivity of the lithospheric mantle. We use $k_m = 3 \text{ W m}^{-1} \text{ K}^{-1}$, a value appropriate for mantle rocks at temperatures of at least several hundred degrees Celsius^{67,69}, as expected at the upper mantle of Venus.

This forward model allows us to calculate T_e^* from T_c and F_s . We can then compare T_e^* with observed T_e in combination with T_c estimates to put constraints on F_s , considering uncertainties in each estimated value. We use a Monte Carlo method to sample T_c and T_e within their respective uncertainty bounds and minimize the squared difference between calculated and estimated T_e . T_c and T_e values are extracted from the models described in the previous section and averaged onto $2^\circ \times 2^\circ$ grids. The range of acceptable values is thus determined by the distribution of F_s that fits both T_c and T_e within uncertainties. The method is applied at each grid point. The standard deviation of the heat flow results is shown in Fig. S2b.

Radioactive heat production

The radioactive heat production of the Venusian crust, as well as its vertical or regional variations, is poorly known. There are five surface measurements of heat-producing elements (HPEs) abundances from Venera 8, 9 and 10, and Vega 1 and 2 landers^{31,32}. If the discrepant measurements by Venera 8 are discarded, then mean abundances for Th, U and K are, respectively, 2 ppm, 0.6 ppm, and 0.4 percent. We calculated heat production rates using the decay constants of Van Schmus⁷⁰, obtaining heat production rates of $0.36\text{-}0.44 \mu\text{W m}^{-3}$ for the age range between the present-day and 1000 Ma. We, therefore, use a value of $0.4 \mu\text{W m}^{-3}$ in our heat flow calculations. Considering that the vertical distribution of HPEs in the Venusian crust is unknown, this value is useful for our study.

Earth heat flow map

We use the terrestrial heat flow data set of Lucazeau² to construct the global heat flow map of the Earth presented in Figure 2b. The original data were averaged onto a $2^\circ \times$

2° grid for comparison with our results. The final model varies from a minimum of ~ 28 mW m⁻² to a maximum of ~ 1200 mW m⁻². The global average surface heat flow is ~ 81 mW m⁻², which can be integrated for a sphere with a mean radius of 6371 km to give a total heat loss of 41 TW. Note that the terrestrial map was based on heat flow measurements instead of T_e -derived estimates, and for this reason the amplitude of heat flow values is higher. However, the geographical pattern shown in this map is consistent with several geophysical proxies².

Total heat loss

We calculate the total surface heat loss implied by our heat flow map by adding the contribution of all the $2^\circ \times 2^\circ$ pixels in the grid. The contribution of each pixel is given by multiplying heat flow by pixel area (which depends on latitude). This gives the heat loss expressed in power units^{1,2}. We calculate the total mantle heat loss by subtracting the crustal contribution from the surface heat loss. An upper limit to the mantle heat loss is obtained if crustal heat sources are not considered.

Total radioactive heat production

We calculate a range for the present-day radioactive heat production of Venus from mass-scaling of terrestrial values. The uncompressed densities of Venus and Earth are similar, so Earth can be considered a good model for Venus. The terrestrial total heat production is not well constrained, and the proposed values rely on the compositional model. We here consider four possible compositional models: the CI chondrite-constrained model of McDonough and Sun³⁸, the pyrolite model of Lyubetskaya and Korenaga³⁹, the Enstatite chondrite-based model of Javoy and Kaminski⁴¹, and the model of Jackson and Jellinek⁴⁰ based on the geochemistry of Nd and Sm. The respective total heat production of these models ranges from 19.8 to 13.7 TW (see ref. 41), values that we scaled directly to the mass of Venus.

Basalt melting and basalt/eclogite transition

To evaluate the possibility of large-scale basalt melting or crustal eclogitization, we compare crustal temperatures with the solidus and liquidus temperatures and the temperature for the basalt/eclogite transition. Basalt solidus⁷¹ and liquidus⁷² temperatures are calculated as a function of pressure from, respectively, $T_{solidus}$ (K) = $1330 + 0.075P$, and $T_{liquidus}$ (K) = $1423 + 0.105P$, where P is the pressure given in MPa. The relation between temperature and pressure for the basalt-eclogite transition has been calculated using data from Herzog et al.⁷³.

REFERENCES

1. Davies, J.H., Davies, D.R. Earth's surface heat flux. *Solid Earth* **1**, 5–24 (2010).
2. Lucazeau, F. Analysis and mapping of an updated terrestrial heat flow data set. *Geochemistry, Geophysics, Geosystems* **20**, 4001–4024 (2019).
3. Rolf, T., et al. Dynamics and evolution of Venus' mantle through time. *Space Science Reviews* **218**, 70 (2022).
4. Noack, L., Breuer, D. & Spohn, T. Coupling the atmosphere with interior dynamics: implications for the resurfacing of Venus. *Icarus* **217**, 484–498 (2012).
5. Moore, W. B., Simon, J. I. & Webb, A. A. G. Heat-pipe planets. *Earth Planet. Sci. Lett.* **474**, 13–19 (2017).
6. Lourenço, D.L., Rozel, A.B., Ballmer, M.D., & Tackley, P. J. Plutonic-squishy lid: a new global tectonic regime generated by intrusive magmatism on Earth-like planets. *Geochem. Geophys. Geosyst.* **21**, e2019GC008756 (2020).
7. Turcotte, D.L. An episodic hypothesis for Venusian tectonics. *J. Geophys. Res.* **98**, 17061-17068 (1993).
8. Uppalapati, S., Rolf, T., Cramer, F., & Werner, S.C. Dynamics of lithospheric overturns and implications for Venus's surface. *J. Geophys. Res. Planets* **125**, e2019JE006258 (2020).
9. Lenardic, A. The diversity of tectonic modes and thoughts about transitions between them. *Phil. Trans. R. Soc. A* **376**, 20170416 (2018).
10. Weller, M.B. & Kiefer, W.S. The physics of changing tectonic regimes: implications for the temporal evolution of mantle convection and the thermal history of Venus. *J. Geophys. Res. Planets* **125**, e2019JE005960 (2020).
11. Tian, J., Tackley, P.J. & Lourenço, D.L. The tectonics and volcanism of Venus: New modes facilitated by realistic crustal rheology and intrusive magmatism. *Icarus* **399**, 115539 (2023).
12. Weller, M.B., Evans, A.J., Ibarra, D.E. & Johnson, A.V. Venus's atmospheric nitrogen explained by ancient plate tectonics. *Nat Astron* (2023). <https://doi.org/10.1038/s41550-023-02102-w>.
13. Marchi, S., Rufu, R. & Korenaga, J. Long-lived volcanic resurfacing of Venus driven by early collisions. *Nat Astron* **7**, 1180-1187 (2023). <https://doi.org/10.1038/s41550-023-02037-2>
14. Phillips, R. J. et al. Lithospheric mechanics and dynamics of Venus, in *Venus II* (ed. Bougher, S.W., Hunten, D.M. & Phillips, R.J.), 1163–1204 (University of Arizona Press, 1997)
15. O'Rourke, J. G., & Smrekar, S. E. Signatures of lithospheric flexure and elevated heat flow in stereo topography at coronae on Venus. *J. Geophys. Res. Planets* **123**, 369–389 (2018).
16. Borrelli, M.E., O'Rourke, J.G., Smrekar, S.E., Ostberg, C.M. A global survey of lithospheric flexure at steep-sided domical volcanoes on Venus reveals intermediate elastic thicknesses. *J. Geophys. Res. Planets* **126**, e06756 (2021).
17. Maia, J. S., & Wiczorek, M. A. (2022). Lithospheric structure of Venusian crustal plateaus. *J. Geophys. Res. Planets* **127**, e2021JE007004 (2022).
18. Smrekar, S.E., Ostberg, C., O'Rourke, J.G. Earth-like lithospheric thickness and heat

- flow on Venus consistent with active rifting. *Nature Geoscience* **16**, 13–18 (2023).
19. Gilmore, M.S. et al. Style and sequence of extensional features in tessera terrain. Venus. *J. Geophys. Res.* **103**, 16813–16840 (1998).
 20. Ruiz, J. The heat flow during the formation of ribbon terrains on Venus. *Planetary and Space Science* **55**, 2063–2070 (2007).
 21. Moruzzi, S.A., Kiefer, W.S., Andrews-Hanna, J.C. Thrust faulting on Venus: Tectonic modeling of the Vedma Dorsa Ridge Belt, *Icarus* **392**, 115378 (2023).
 22. Bjornes, E., Johnson, B. C., Evans, A. J. Estimating Venusian thermal conditions using multiring basin morphology. *Nature Astronomy* **5**, 498–502 (2021).
 23. Nimmo, F., Mackwel, S., Viscous relaxation as a probe of heat flux and crustal plateau composition on Venus. *PNAS* **120**, e2216311120 (2023).
 24. Solomon, S.C., Head, J.W. Mechanics for lithospheric heat transport on Venus: implications for tectonic style and volcanism. *J. Geophys. Res.* **87**, 9236–9246 (1982).
 25. Turcotte, D.L. How does Venus lose heat? *J. Geophys. Res.* **100**, 16,931–16,940 (1995).
 26. Brown, C.D., Grimm, R.E. Recent tectonic and lithospheric thermal evolution of Venus. *Icarus* **139**, 40–48 (1999).
 27. McKinnon, W.B., Zahnle, K.J., Ivanov, B.A., & Melosh, H. J. (1997). Cratering on Venus: Models and observations, in *Venus II* (ed. Bougher, S.W., Hunten, D.M. & Phillips, R.J.), 1047–1086 (University of Arizona Press, 1997).
 28. Jimenez-Diaz, A. et al. Lithospheric structure of Venus from gravity and topography. *Icarus* **260**, 215–231 (2015).
 29. McNutt, M. K. Lithospheric flexure and thermal anomalies. *J. Geophys. Res.* **89**, 11180–11194 (1984).
 30. Ruiz, J. et al. The thermal evolution of Mars as constrained by paleo-heat flows. *Icarus* **215**, 508–517 (2011).
 31. Surkov, Y.A., et al.(1984) New data on the composition, structure, and properties of Venus rock obtained by Venera-13 and Venera-14. *J. Geophys. Res.* **89**, B393–B402 (1984).
 32. Surkov Y.A., et al. Venus rock composition at the Vega-2 landing site. *J. Geophys. Res.* **91**, B215–B218 (1986).
 33. Romeo, I., Turcotte, D.L. Pulsating continents on Venus: An explanation for crustal plateaus and tessera terrains. *Earth Planet. Sci. Lett.* **276**, 85–97 (2008).
 34. Hashimoto, G.L. et al. Felsic highland crust on Venus suggested by galileo near-infrared mapping spectrometer data. *J. Geophys. Res.* **113**, E00B24 (2008).
 35. Gilmore, M., Treiman A., Helbert, J., Smrekar, S. Venus surface composition constrained by observation and experiment. *Space Sci. Rev.* **212**, 1511–1540 (2017).
 36. Surkov Y.A., et al. Uranium, thorium, and potassium in the Venusian rocks at the landing sites of Vega-1 and Vega-2. *J. Geophys. Res.* **92**, B537–B540 (1987).
 37. Crumpler, L S., Head, J. W., & Aubele, J.C. Relation of major volcanic center concentration on Venus to global tectonic patterns. *Science* **261**, 591–595 (1993).
 38. McDonough, W.F., Sun, S.-s. The composition of the Earth. *Chem. Geol.* **120**, 223–253 (1995).
 39. Lyubetskaya, T., Korenaga, J. Chemical composition of Earth’s primitive mantle and its variance: 1. Methods and results. *J. Geophys. Res.* **112**, B03211 (2007).

40. Jackson, M.G., Jellinek, A.M. Major and trace element composition of the high $^3\text{He}/^4\text{He}$ mantle: Implications for the composition of a nonchondritic Earth. *Geochem. Geophys. Geosyst.* **14**, 2954–2976 (2013).
41. Javoy, M., Kaminski, E. Earth's Uranium and Thorium content and geoneutrinos fluxes based on enstatite chondrites. *Earth Planet. Sci. Lett.* **407**, 1–8 (2014).
42. Korenaga, J. Urey ratio and the structure and evolution of Earth's mantle. *Rev. Geophys.* **46**, RG2007 (2008).
43. Adams, A.C., Stegman, D.R., Smrekar, S.E., & Tackley, P.J. Regional-scale lithospheric recycling on Venus via peel-back delamination. *J. Geophys. Res. Planets* **127**, e2022JE007460 (2022).
44. Watts, A.B., Burov, E.B. Lithospheric strength and its relation to the elastic and seismogenetic layer thickness. *Earth Planet. Sci. Lett.* **213**, 113–131 (2003).
45. McGovern, P.J., et al. Localized gravity/topography admittance and correlation spectra on Mars: Implications for regional and global evolution. *J. Geophys. Res.* **107**, 5136, (2002).
46. Jellinek, A.M., Jackson, M.G. Connections between the bulk composition, geodynamics and habitability of Earth. *Nature Geoscience* **8**, 587-593 (2015).
47. Ruiz, J. Heat flow evolution of the Earth from paleomantle temperatures: Evidence for increasing heat loss since ~2.5 Ga. *Physics of the Earth and Planetary Interiors* **269**, 165-171, (2017).
48. Kearey, P., Klepeis, K., Vine, F.J. *Global tectonics*. Wiley-Blackwell, (2009).
49. Davaille, A., Smrekar, S.E., Tomlinson, S. Experimental and observational evidence for plume-induced subduction on Venus. *Nature Geoscience* **10**, 349-355 (2017).
50. Wieczorek, M.A. *Gravity and topography of the terrestrial planets* (Elsevier, Oxford, 2015).
51. Rappaport, N.J., Konopliv, A.S., Kucinskis, A.B. An improved 360 degree and order model of Venus topography. *Icarus* **139**, 19-31 (1999).
52. Konopliv, A.S., Banerdt, W.B., Sjogren, W.L. Venus gravity: 180th degree and order model. *Icarus* **139**, 3-18 (1999).
53. Wieczorek, M.A., Phillips, R.J.. Potential anomalies on a sphere: Applications to the thickness of the lunar crust. *J. Geophys. Res.* **103**, 1715–1724 (1998).
54. Regorda, A., Thieulot, C., van Zelst, I., Erdős, Z., Maia, J., & Buiters, S. (2023). Rifting Venus: Insights from numerical modeling. *J. Geophys. Res. Planets* **128**, e2022JE007588.
55. Kirby, J.F., Swain, C.J. A reassessment of spectral Te estimation in continental interiors: the case of North America. *J. Geophys. Res.* **114**, B08401 (2009).
56. Kirby, J.F., Swain, C.J. Improving the spatial resolution of effective elastic thickness estimation with the fan wavelet transform. *Computers & Geosciences* **37**, 1345–1354 (2011).
57. Forsyth, D.W. Subsurface loading estimates of the flexural rigidity of continental lithosphere. *J. Geophys. Res.* **90**, 12,623–12,632 (1985).
58. Burov, E.B., Diament, M. The effective elastic thickness (T_e) of continental lithosphere: What does it really mean? *J. Geophys. Res.* **100**, 3905–3927 (1995).
59. Ranalli, G. *Rheology of the Earth* (Chapman and Hall, London, 1995).
60. Tesauro, M. et al. 3D strength and gravity anomalies of the European lithosphere.

- Earth Planet. Sci. Lett.* **263**, 56–73 (2007).
61. Grimm, R.E. Recent deformation rates on Venus. *J. Geophys. Res.* **99**, 23163–23171 (1994).
 62. Ranalli, G. Nonlinear flexure and equivalent mechanical thickness of the lithosphere. *Tectonophysics* **240**, 107–114 (1994).
 63. Mackwell, S.J., Zimmerman, M.E., Kohlstedt, D.L. High temperature deformation of dry diabase with application to tectonics on Venus. *J. Geophys. Res.* **103**, 975–984 (1998).
 64. Chopra, P.N., Paterson, M.S. The role of water in the deformation of dunite. *J. Geophys. Res.* **89**, 7861–7876 (1984).
 65. Burov, E.B., Diament, M. Flexure of the continental lithosphere with multilayered rheology. *Geophys. J. Int.* **109**, 449–468 (1992).
 66. Beardmore, G.R., Cull, J.P. *Crustal Heat Flow: A Guide to Measurement and Modelling* (Cambridge University Press, Cambridge, 2001).
 67. Vosteen, H.D. & Schellschmidt, R. Influence of temperature on thermal conductivity, thermal capacity and thermal diffusivity for different types of rock. *Physics and Chemistry of the Earth* **28**, 499–509 (2003).
 68. Miao, S.Q., Li, H.P. & Chen, G. Temperature dependence of thermal diffusivity, specific heat capacity, and thermal conductivity for several types of rocks. *J Therm Anal Calorim* **115**, 1057–1063 (2014).
 69. McKenzie, D., Jackson, J., Priestley, K. Thermal structure of oceanic and continental lithosphere. *Earth Planet. Sci. Lett.* **233**, 337–349 (2005).
 70. Van Schmus, W.R. Natural radioactivity of the crust and mantle, in *Global Earth physics: A handbook of physical constants* (ed. Ahrens, T.J.), 283–291 (American Geophysical Union, 1995).
 71. Yasuda, A., Fujii, T., Kurita, K. Meeting phase relations of an anhydrous mid-ocean ridge basalt from 3 to 20 GPa: implications for the behavior of subducted oceanic crust in the mantle. *J. Geophys. Res.* **99**, 9401–9414 (1994).
 72. Schmidt, M.W., Poli, S. Experimentally based water budgets for dehydrating slabs and consequences for arc magma generation. *Earth Planet. Sci. Lett.* **163**, 361–379 (1998).
 73. Herzog, S.G., Hess, P.C., Parmentier, E.M.. Constraints on the basalt to eclogite transition and crustal recycling on Venus. *Lunar and Planetary Science Conference* **26**, 591, (1995).

ACKNOWLEDGEMENTS

This work was supported by funding from the Spanish Agencia Estatal de Investigación through the project PID2022-140686NB-I00 (MARVEN).

DATA AVAILABILITY

The digital models for crustal thickness, effective elastic thickness and heat flow will be publicly available from <https://zenodo.org>

AUTHOR CONTRIBUTIONS

J.R. designed the research, calculated heat production and global heat budget, and wrote the first draft of the main manuscript. P.A., A.J.-D., I.E.-G. and J.R. designed the methodology. P.A. and J.R. conceptualized the model relating heat flow and elastic thickness data. A.J.-D. managed crustal and elastic thickness data and performed the heat flow calculations. J.R., A.J.-D, and I.R. interpreted heat flow results. A.J.-D. and I.E.-G. analyzed temperature profiles and large-scale stability of the crust. J.R. and I.R. managed funding acquisition. All authors discussed the results and contributed to the final manuscript. This paper is dedicated to the memory of Blanqui L.R.

COMPETING INTERESTS

The authors declare no competing interests.

FIGURE LEGENDS

Figure 1. Topography and effective elastic thickness maps for Venus. (a) Topography map of Venus (model VenusTopo719; ref. 50), with names of the main regions of Venus, and (b) Global map of the effective elastic thickness (T_e) of Venus with a resolution of $2^\circ \times 2^\circ$; the total T_e range is between 4.8 and 105 km. The uncertainty in the estimate of T_e is shown in Fig. S2a. All the maps appear in a Robinson projection; the central meridian corresponds to the 180°E longitude. See Methods for details.

Figure 2. Global heat flow maps for Venus and Earth. (a) Global map of the heat flow of Venus obtained from the effective elastic thickness of the lithosphere (T_e). The map resolution is $2^\circ \times 2^\circ$. The heat flow pattern is relatively smooth, with the ratio between maximum and minimum values lower than ten, although there are large-scale areas concentrating high and low heat flows. The uncertainty in heat flow estimates is shown in Fig. S2b. (b) Global map of the surface heat flow of Earth, constructed from the more recent heat flow database², shown at the same resolution. There is a clear relation between plate tectonic features and heat flow: highs are related to mid-ocean spreading ridges, whereas lows occur in old continental interiors, with a ratio between maximum and minimum values being much higher than ten. Each map has its own color scale for visualization purposes. Fig. S6 shows the same maps but with a common color scale to emphasize the differences in absolute value between both planets. The central meridian corresponds to the 180°E longitude for Venus, and 0° for Earth.

Figure 3. Crustal temperatures compared with conditions for basalt melting and eclogitization. (a) Colored dots indicate temperatures at the base of the crust derived from our heat flow results (see Fig. S3), compared with the conditions for solidus (melt initiation), liquidus (melt completion) and eclogitization of basalts (see Methods). Eclogitization is unexpected, and only a few temperatures at the base of the crust-crustal thickness points exceed solidus and liquidus conditions (43 and 15 points, respectively, on a total of 15692 points; see also Figs. S4a and S4b).

Figure 4. Total heat loss and heat budget of Venus. (a) The inverse of the Urey ratio (Ur) for bulk Venus. Ur^{-1} gives the proportion between the total heat loss and the total heat production. It provides a direct representation of the heat budget of the planet and its implications for interior (considered as a whole) cooling or heating. Ur^{-1} has been calculated from mass-scaling relations from a range of possible compositional models for Earth. The red curve represents our nominal heat loss of 14.0 TW, whereas the dark red curve represents the extreme case for a heat loss of 14.5 TW; both curves are calculated considering a radiogenic crustal heat production of $0.4 \mu\text{W m}^{-3}$ (see Methods). For comparison, the blue curve represents the case without considering heat sources, which gives a total heat loss of 11.0 TW. The horizontal black line has been included to show the $Ur^{-1} = 1$ case. (b) Total surface and mantle heat loss in terms of the crustal heat production; for the highest heat production considered, $0.4 \mu\text{W m}^{-3}$, the heat loss was set to our nominal value of 14 TW. The mantle heat loss is not very sensitive to crustal heat production.

Figure S1. Crustal thickness model for Venus. Crustal thickness model used in our analysis. The model is based on Jiménez-Díaz et al.²⁸, assumes a mean crustal thickness of 25 km, crust and mantle densities of, respectively, 2900 and 3300 kg m⁻³, and has been averaged onto a 2° × 2° grid. The central meridian corresponds to the 180°E longitude.

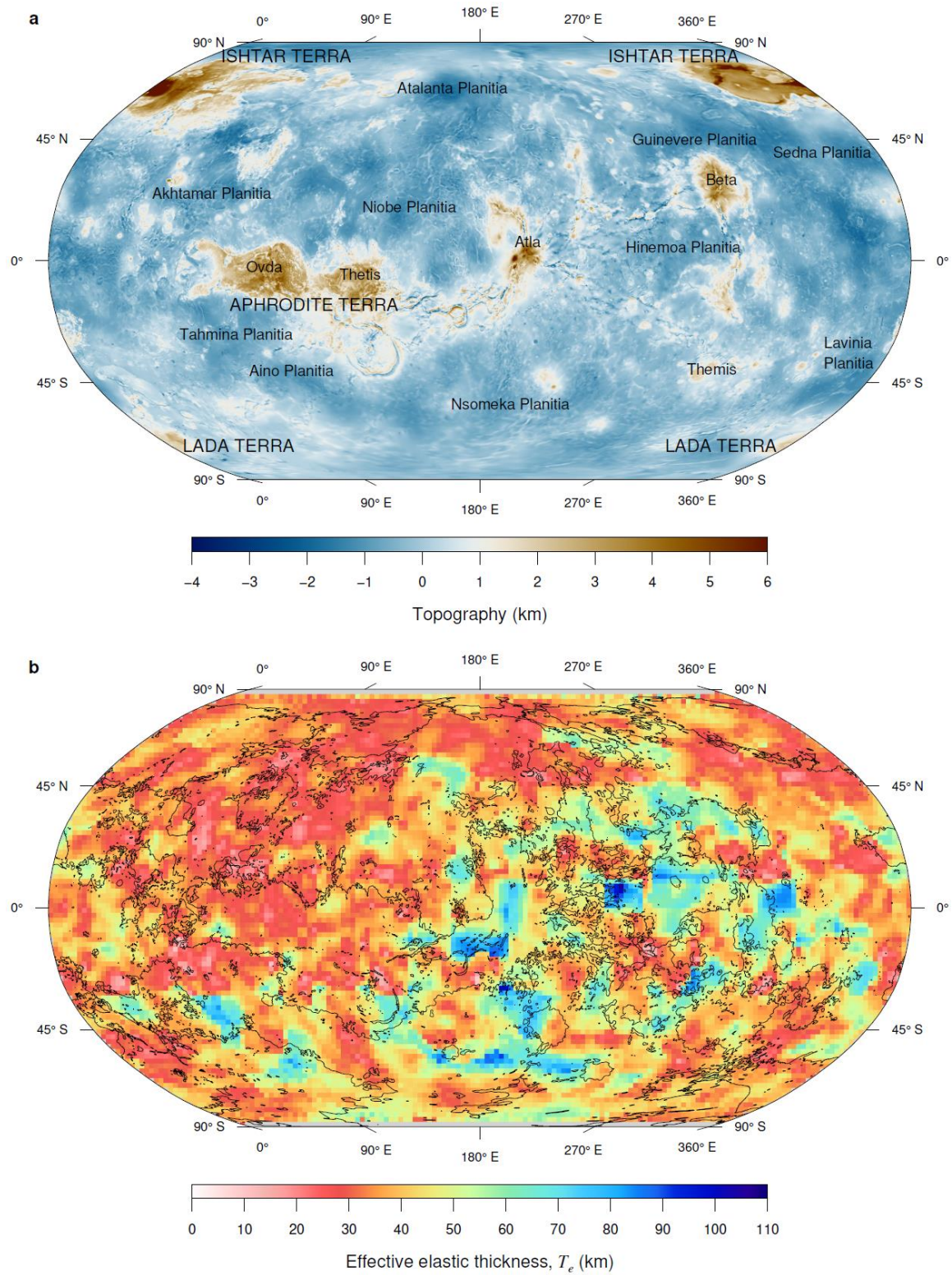
Figure S2. Uncertainty in effective elastic thickness and heat flow estimates. (a) Error in the determination of T_e given as 95% confidence limits on the best-fitting value. (b) Standard deviation of the calculated heat flow derived from the uncertainty in the determination of T_e .

Figure S3. Temperature at the base of the crust. Global map of temperatures at the base of the crust obtained from our heat flow map.

Figure S4. Basalt melting conditions in the base of the crust. (a) Difference between the temperature at the base of the crust and the local solidus temperature for the 43 pixels for which solidus conditions are reached; the rest of the map is masked by clarity. (b) Difference between the temperature at the base of the crust and the local liquidus temperature for the 15 pixels for which liquidus conditions are reached, with the rest of the maps masked for clarity. The total number of pixels in the grid is 15,692. The central meridian corresponds to the 180°E longitude.

Figure S5. Urey ratio for bulk Venus. The Urey ratio represents a common way of showing a planet's global heat budget. The represented values are the inverse of those shown in Fig. 4a. The horizontal black line indicates the $Ur = 1$ case.

Figure S6. Global heat flow maps for Venus and Earth at the same color scale. Global 2° × 2° maps of the heat flow of (a) Venus and (b) Earth, constructed as shown in Figure 2, but represented with a common colour scale to emphasize the differences in absolute value between both planets. Due to the larger range in terrestrial values, Venesian features show less color differences, even with a saturation value of 110 mW m⁻². The central meridian corresponds to the 180°E longitude for Venus, and 0° for Earth.



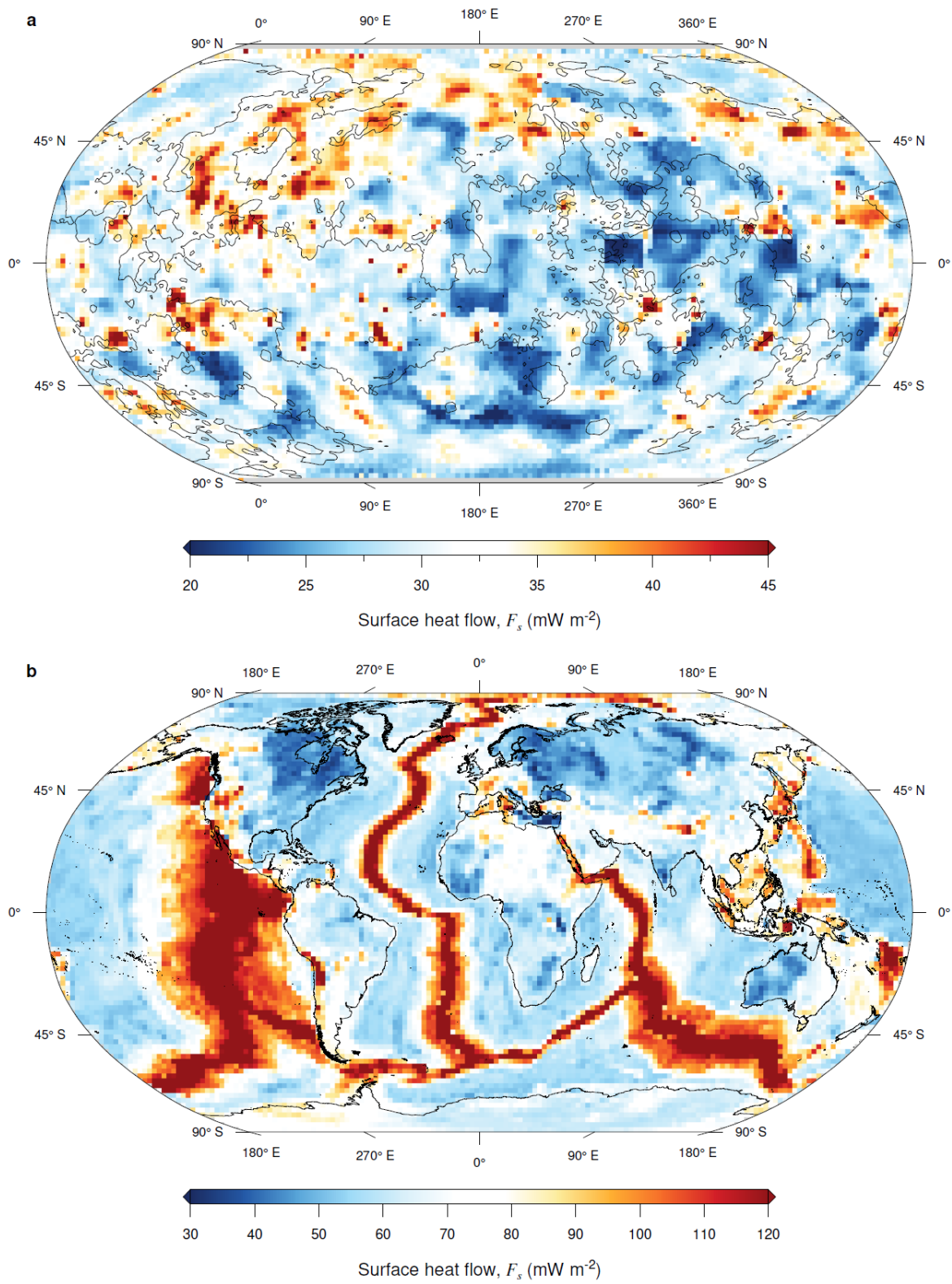


FIGURE 2

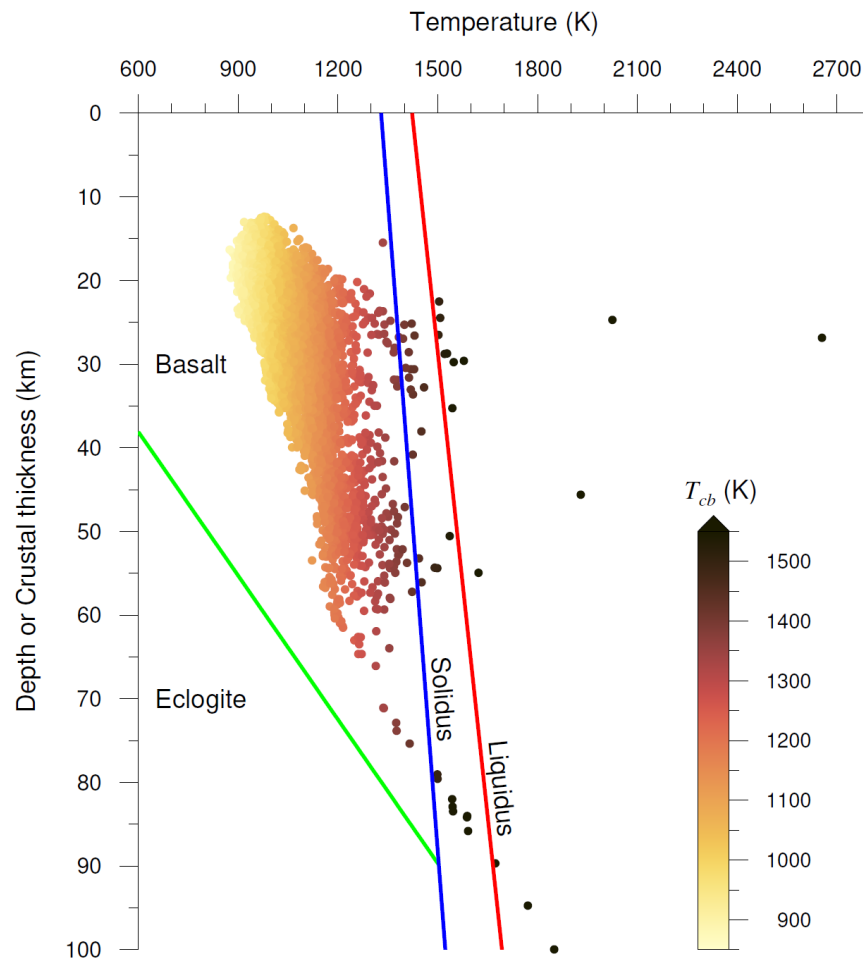


FIGURE 3

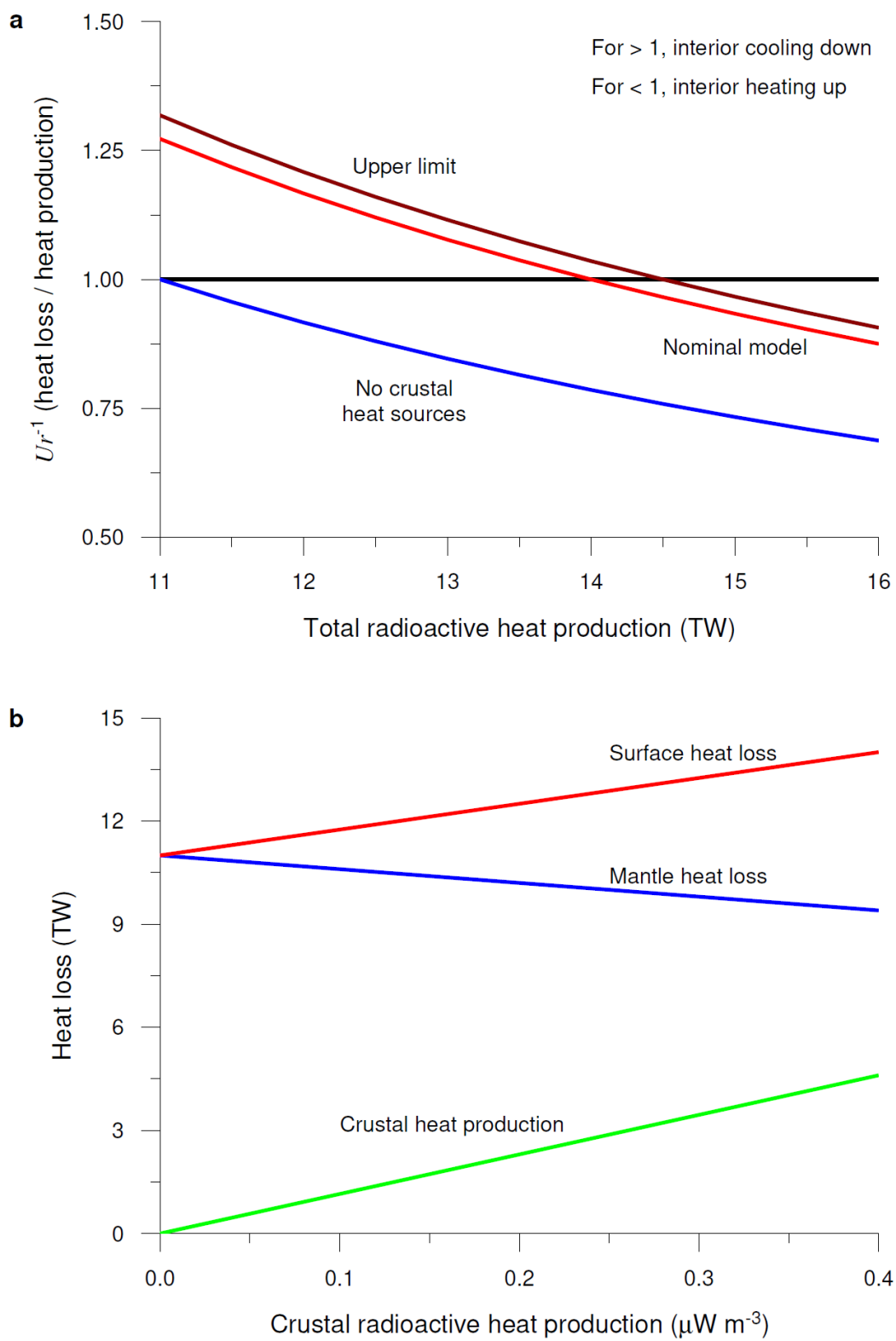
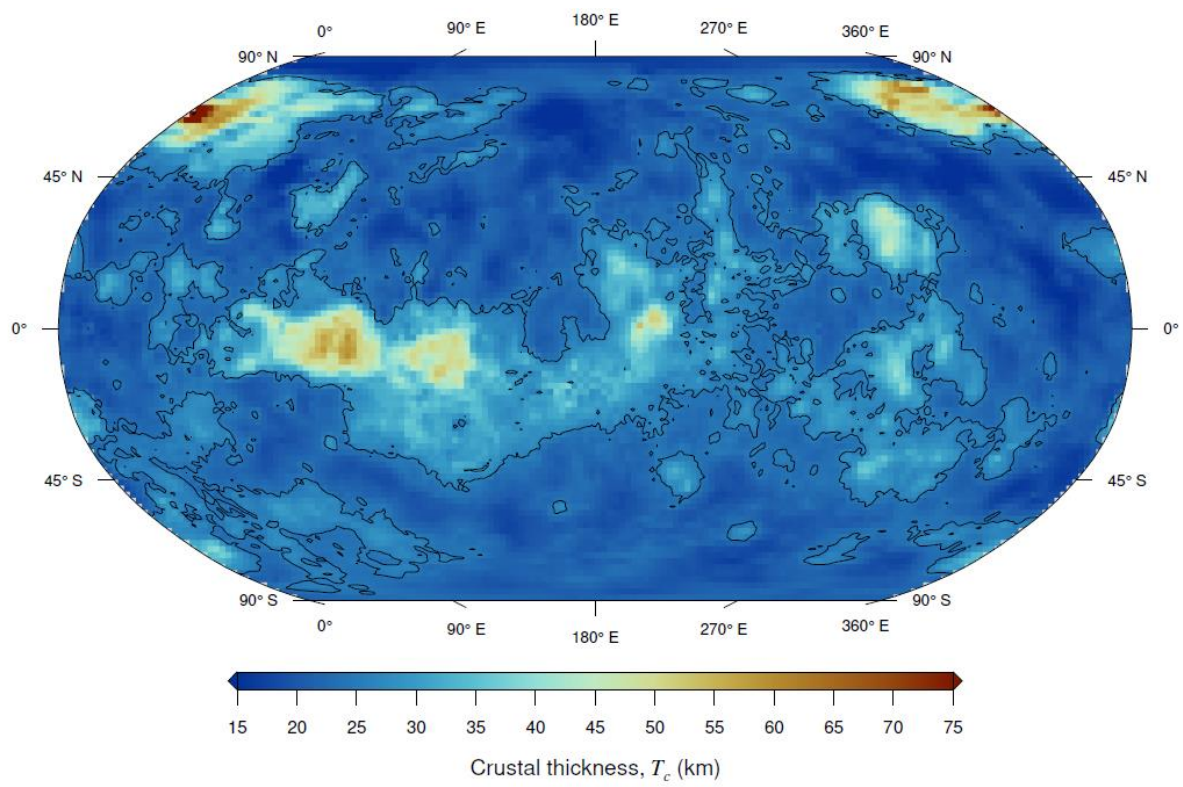


FIGURE 4

**FIGURE S1**

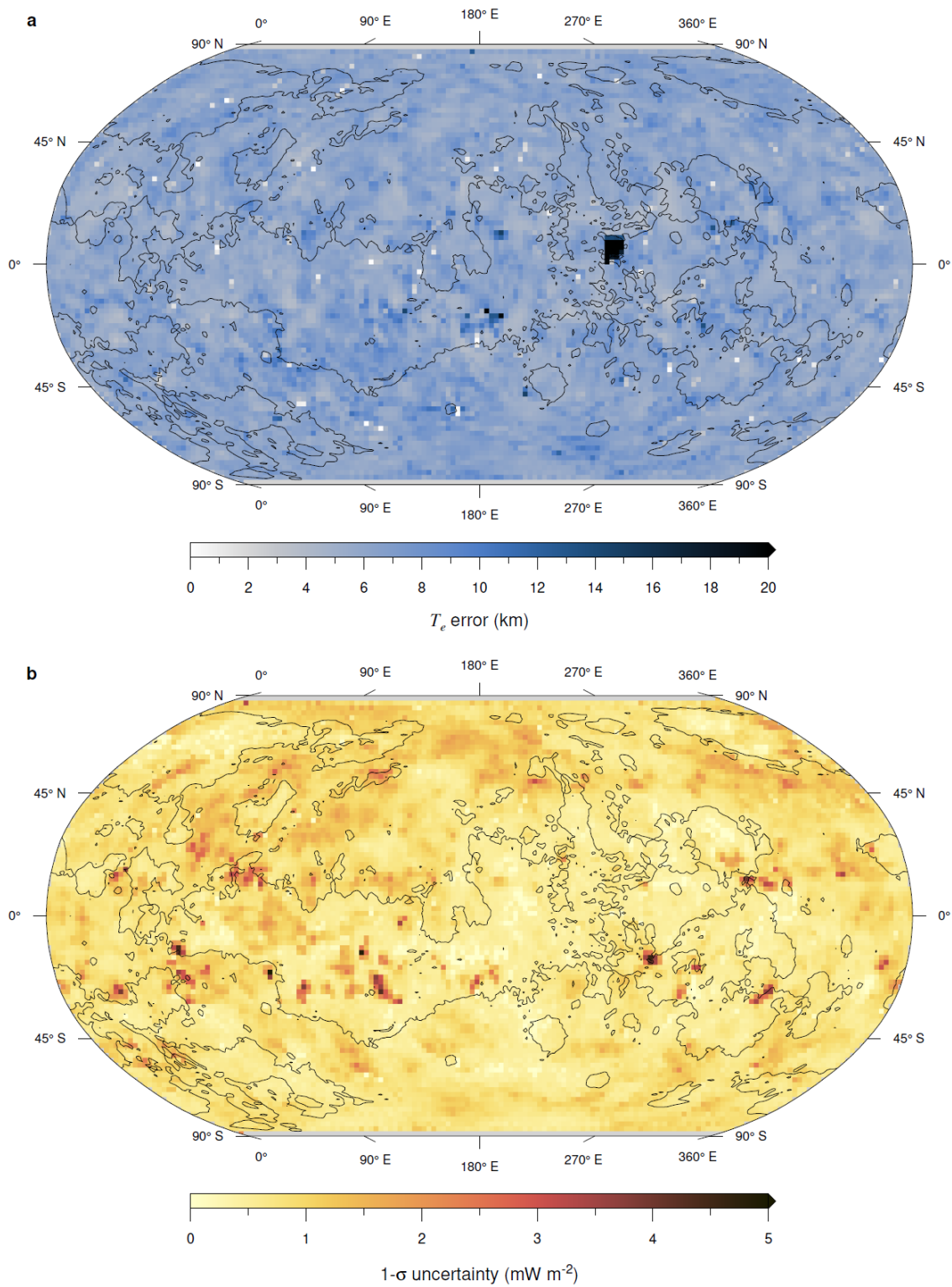
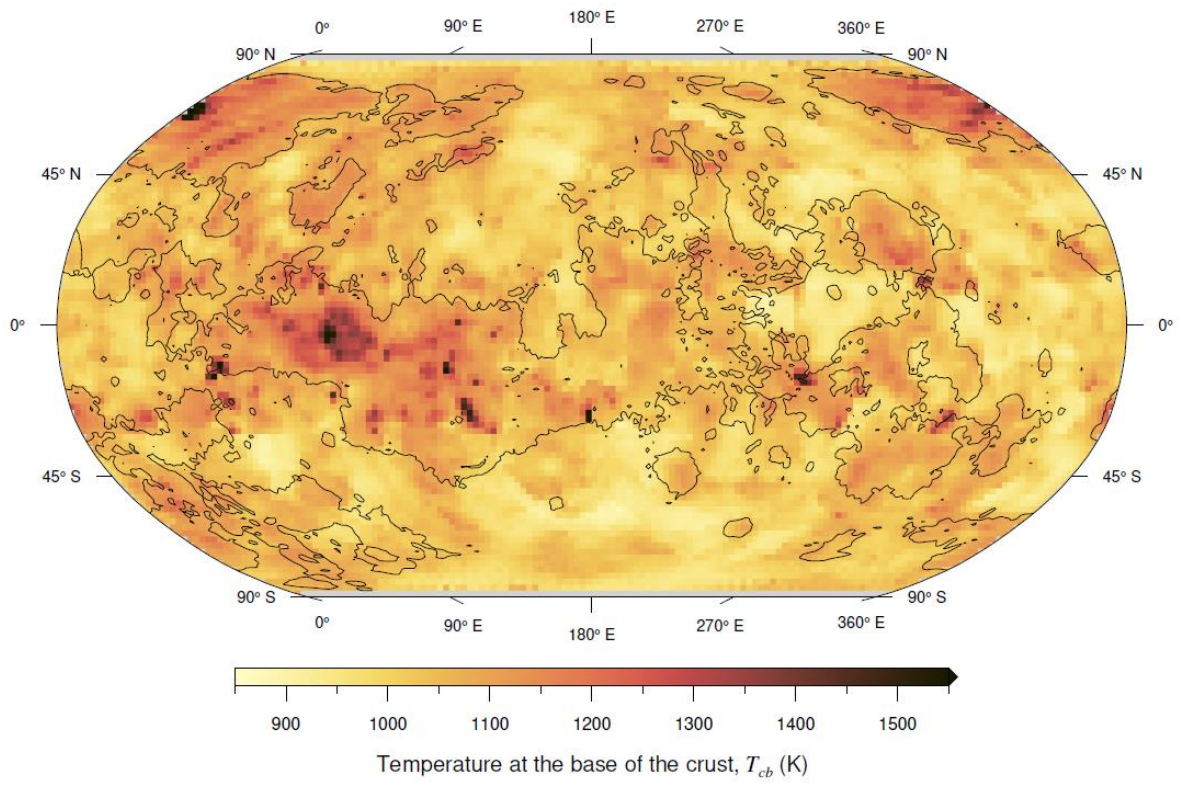


FIGURE S2

**FIGURE S3**

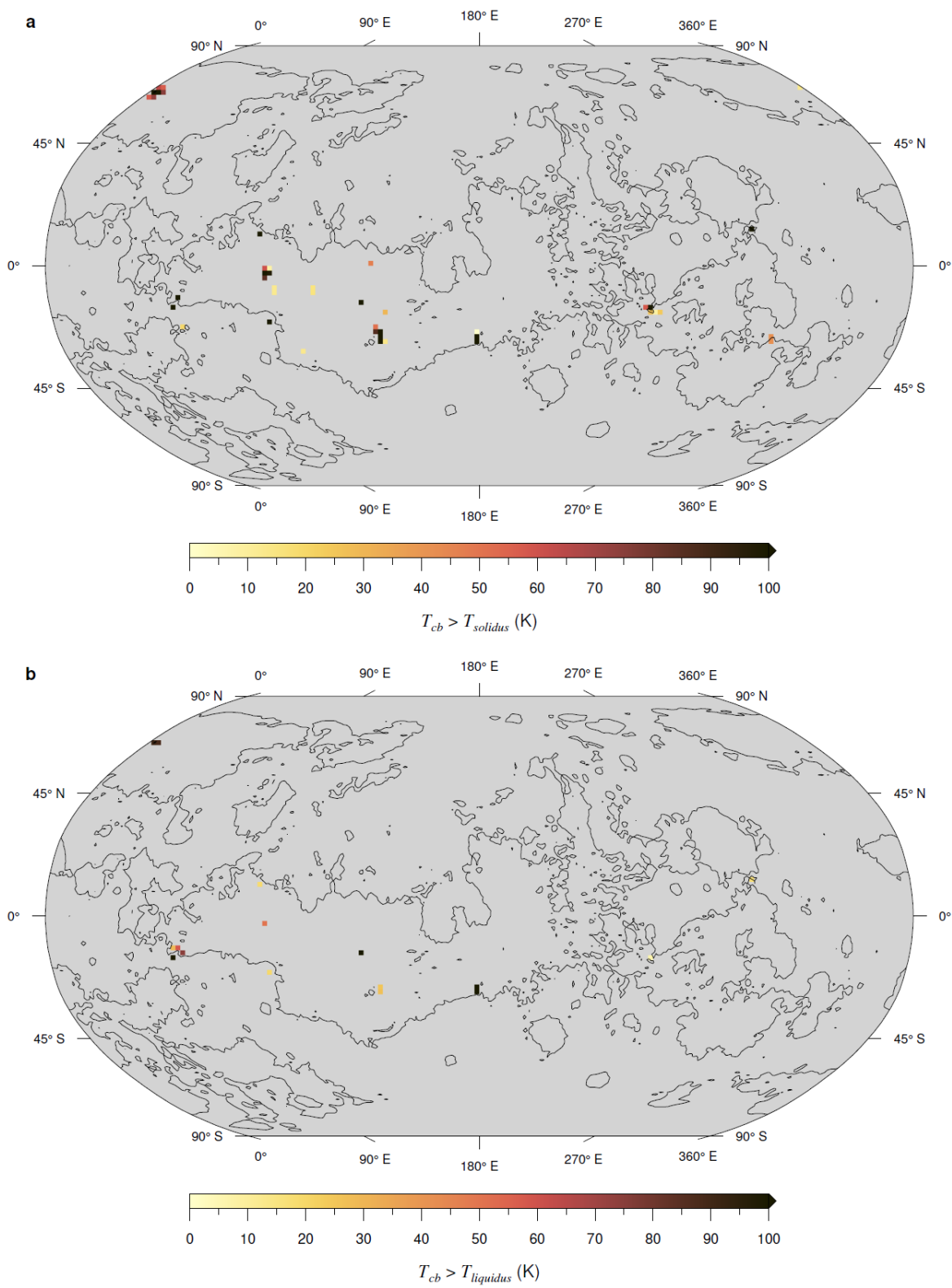
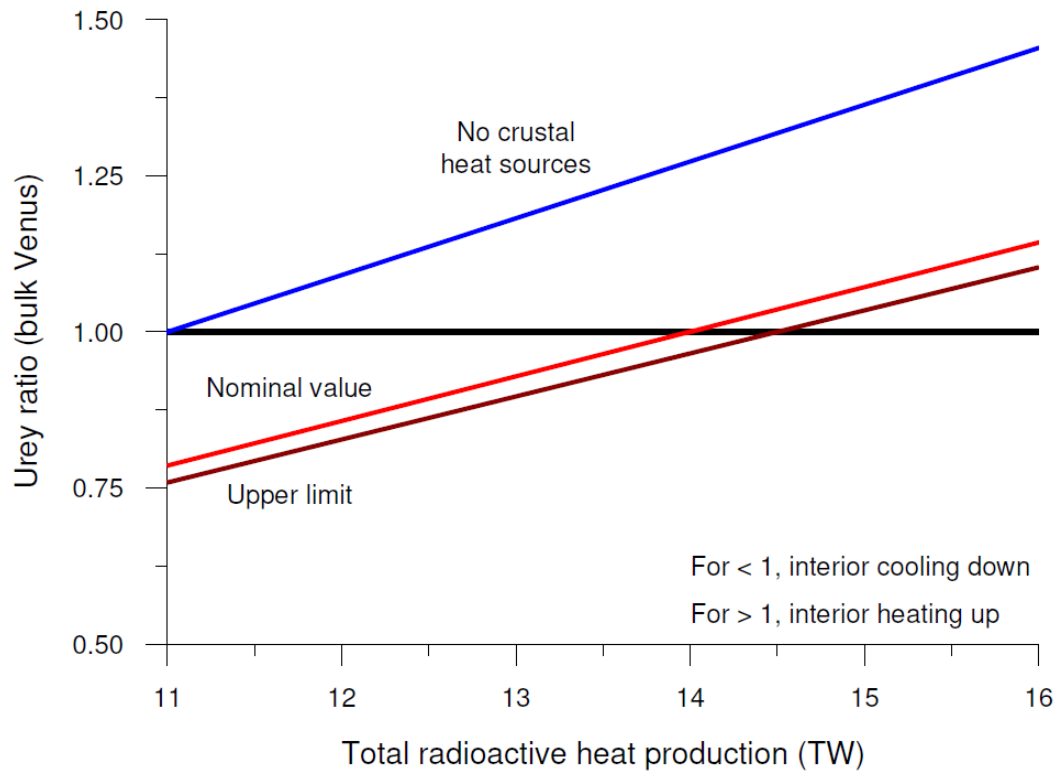
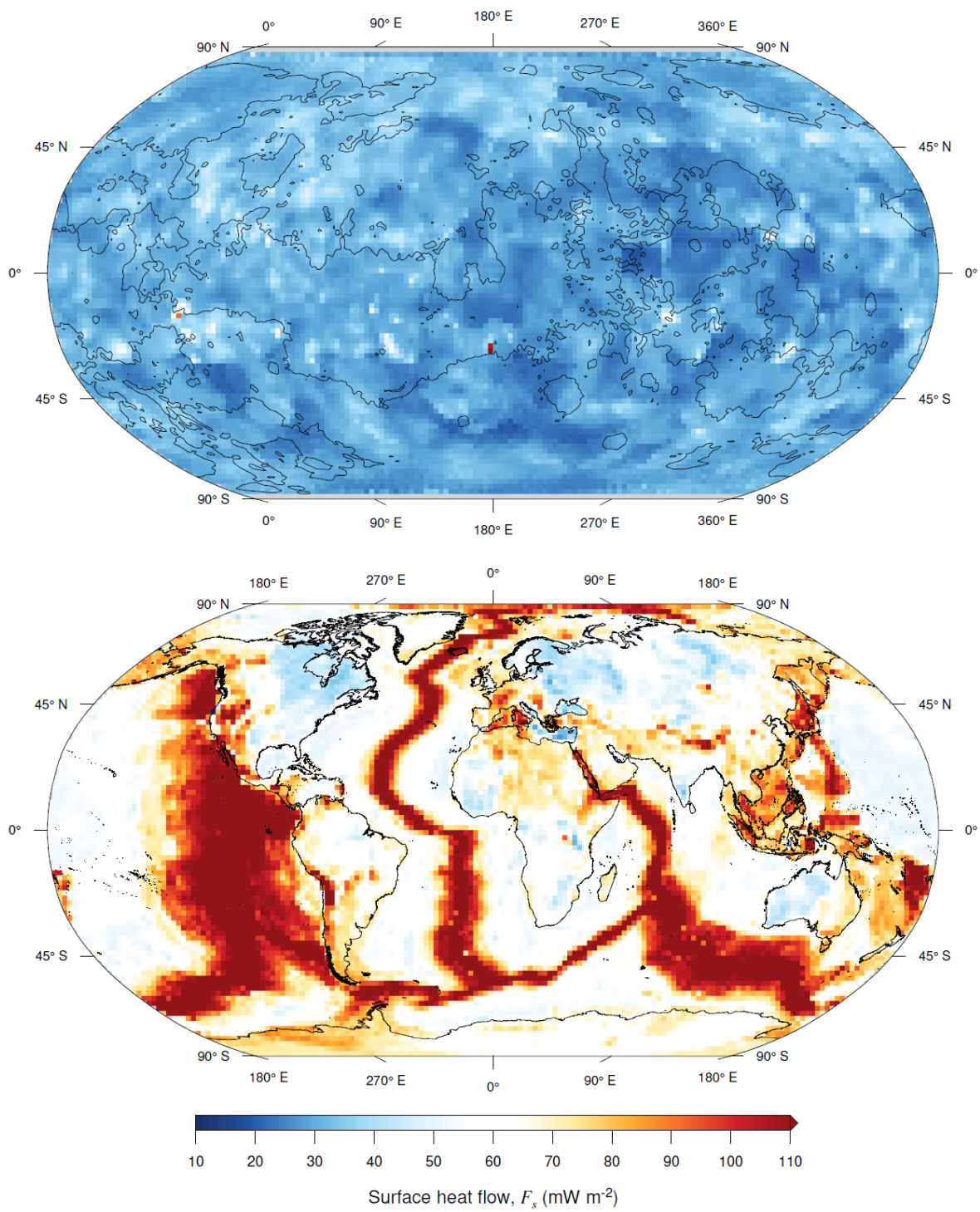


FIGURE S4

**FIGURE S5**

**FIGURE S6**